Composite flexible skin with large negative Poisson's ratio range: numerical and experimental analysis

2013 Smart Mater. Struct. 22 045005

(http://iopscience.iop.org/0964-1726/22/4/045005)

Smart Mater. Struct. **22** (2013) 045005 (12pp) doi:10.1088/0964-1726/22/4/045005

Composite flexible skin with large negative Poisson's ratio range: numerical and experimental analysis

Y J Chen[1,2], F Scarpa[2,4], I R Farrow[2], Y J Liu[3] and J S Leng[1,4]

[1] Centre for Composite Materials and Structures, Science Park of Harbin Institute of Technology (HIT), No. 2 YiKuang Street, PO Box 3011, Harbin 150080, People's Republic of China
[2] Advanced Composites Centre for Innovation and Science, University of Bristol, Bristol BS8 1TR, UK
[3] Department of Aerospace Science and Mechanics, Harbin Institute of Technology (HIT), No. 92 West dazhi Street, PO Box 301, Harbin, People's Republic of China

E-mail: f.scarpa@bristol.ac.uk and lengjs@hit.edu.cn

Received 31 August 2012, in final form 8 January 2013
Published 26 February 2013
Online at stacks.iop.org/SMS/22/045005

Abstract
This paper describes the manufacturing, characterization and parametric modeling of a novel fiber-reinforced composite flexible skin with in-plane negative Poisson's ratio (auxetic) behavior. The elastic mechanical performance of the auxetic skin is evaluated using a three-dimensional analytical model based on the classical laminate theory (CLT) and Sun's thick laminate theory. Good agreement is observed between in-plane Poisson's ratios and Young's moduli of the composite skin obtained by the theoretical model and the experimental results. A parametric analysis carried out with the validated model shows that significant changes in the in-plane negative Poisson's ratio can be achieved through different combinations of matrix and fiber materials and stacking sequences. It is also possible to identify fiber-reinforced composite skin configurations with the same in-plane auxeticity but different orthotropic stiffness performance, or the same orthotropic stiffness performance but different in-plane auxeticity. The analysis presented in this work provides useful guidelines to develop and manufacture flexible skins with negative Poisson's ratio for applications focused on morphing aircraft wing designs.

(Some figures may appear in colour only in the online journal)

1. Introduction

In recent years, morphing wing technologies have constituted a key design driver to enlarge the flight envelope of aircrafts outside their fixed cruise point, eliminate flap-type mechanisms and reduce aerodynamic drag [1–3]. Traditional aircrafts are designed according to their particular missions, and usually optimized in the most concerned flight performance [4–7]. They can realize the optimal objective through changing their aerodynamic layouts to adapt to the outside flight environment [8–10]. One of the key techniques to realize morphing aircraft is the morphing skin [11, 12], which should have enough strain capability to ensure the changes of camber angle, span length, chord length, sweepback angle and wing area, as well as possessing enough out-of-plane stiffness to maintain the aerodynamics configuration during the deformation process [13]. Meanwhile, in order to reduce the actuation force and power required for morphing, low in-plane stiffness of the morphing skin is also desired during the deformation process [6, 14–16]. The recently emerged composite materials and manufacturing processes open an avenue to the development of morphing skins. A candidate solution proposed is to use sandwiched skins with flexible face-sheets and cellular cores [12, 17, 18].

[4] Authors to whom any correspondence should be addressed.

Cellular and lattice structures have attracted the attention of many researchers around the world for several decades, due to their significant lightweight and out-of-plane stiffness properties [19]. A primary application for cellular solids is their use as sandwich core materials in a variety of engineering technologies, such as marine, aerospace and automotive lightweight structures [20, 21]. The conventional hexagonal honeycomb is a typical example of cellular core configuration, with unit cells made of ribs with equal length and an internal cell angle of $\pi/6$ [22]. Over-expanded center symmetric honeycomb configurations with special orthotropic properties can also be developed when varying the cell wall aspect ratio and internal cell angle, always with positive values [22, 23]. Hexagonal honeycombs with convex configuration (i.e., positive internal cell angle) exhibit anticlastic or saddle-shape curvatures when subject to out-of-plane bending [24–26], making more problematic the use of classical cores in sandwich structures with complex geometry [27]. In contrast, negative Poisson's ratio (auxetic) solids feature synclastic curvature behaviors, making it possible therefore to produce dome-shaped surfaces when bent out-of-plane [25, 28]. Auxetic cellular structures have also been used to prototype morphing wings [7, 29–31], radomes [32], adaptive and deployable structures [33]. Spadoni [34] demonstrated the influence of chiral core geometry on the compliance and confirmed the ability of chiral core airfoils to sustain large deflections while not exceeding yield strain limits. The feasibility of chiral honeycomb used as the airfoil core material was further demonstrated by many other researchers [7, 29, 35]. Furthermore, the re-entrant cellular structures had also been studied as the core materials of airfoils [17, 35, 36]. They also exhibit great potential in the morphing aircraft wing applications.

It is worth noting that most of the previous works were focused on the cellular cores; the face-sheets were not taken into account for simplicity. As a morphing wing skin, it needs to meet the demand of deformation capability, smooth continuous surface and complete air tightness [18]. Therefore, it is necessary to consider the mechanical properties of the face-sheet. For the morphing aircraft wing, if the in-plane Poisson's ratio of the cellular core is different from the face-sheet, this will result in the generation of an internal shear force between the cellular core and face-sheet, and local wrinkling on the face-sheet, which are disadvantageous to the aerodynamic performance of the morphing wing. In order to avoid this problem, a morphing wing composed of a zero-Poisson's ratio honeycomb core and an in-plane zero-Poisson's ratio face-sheet was manufactured and researched by Bubert *et al* [12]. However, the deformability is usually limited in one direction. An alternative method is to design a face-sheet with in-plane negative Poisson's ratio properties.

In this work, a novel flexible composite skin with negative Poisson's ratio has been manufactured and investigated. A three-dimensional theoretical model is presented to describe the mechanical behaviors of the composite skin. The theoretical value of in-plane Poisson's ratio and elastic modulus are verified by experimental results based on in-plane tensile tests. The validated theoretical model has then been used to perform a parametric analysis concerning the dependency of the in-plane Poisson's ratio and elastic modulus versus the different composite material and geometry parameters.

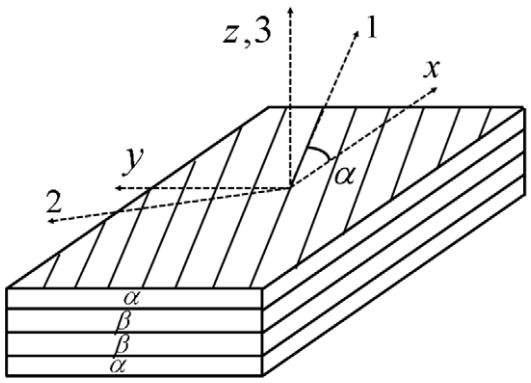

Figure 1. Coordinate relations between material axes (1, 2 and 3) and reference axes (x, y and z).

2. Flexible skin theoretical model

2.1. Flexible skin stress–strain relation

As shown in figure 1, the flexible skin model is considered to be homogeneous anisotropic, with a symmetric but unbalanced fiber orientation $[\alpha/\beta]_S$ with respect to the x direction. For convenience, the Cartesian coordinate system is adopted to analyze the flexible skin. Considering the symmetry properties of the model, the stress–strain relation is expressed in the following form:

$$\begin{Bmatrix} \bar{\sigma}_x \\ \bar{\sigma}_y \\ \bar{\sigma}_z \\ \bar{\tau}_{yz} \\ \bar{\tau}_{zx} \\ \bar{\tau}_{xy} \end{Bmatrix} = \begin{bmatrix} \bar{C}_{11} & \bar{C}_{12} & \bar{C}_{13} & 0 & 0 & \bar{C}_{16} \\ \bar{C}_{12} & \bar{C}_{22} & \bar{C}_{23} & 0 & 0 & \bar{C}_{26} \\ \bar{C}_{13} & \bar{C}_{23} & \bar{C}_{33} & 0 & 0 & \bar{C}_{36} \\ 0 & 0 & 0 & \bar{C}_{44} & \bar{C}_{45} & 0 \\ 0 & 0 & 0 & \bar{C}_{45} & \bar{C}_{55} & 0 \\ \bar{C}_{16} & \bar{C}_{26} & \bar{C}_{36} & 0 & 0 & \bar{C}_{66} \end{bmatrix} \begin{Bmatrix} \bar{\varepsilon}_x \\ \bar{\varepsilon}_y \\ \bar{\varepsilon}_z \\ \bar{\gamma}_{yz} \\ \bar{\gamma}_{zx} \\ \bar{\gamma}_{xy} \end{Bmatrix} \tag{1}$$

where $\bar{C}_{ij}$ $(i, j = 1, 2, 3, 4, 5, 6)$ are the stiffness matrix constants. Once the stiffness matrix $\left[\bar{C}\right]$ is determined, it is possible to obtain a global second-order tensor $[\bar{S}] = [\bar{C}]^{-1}$, where $[\bar{S}]$ is the compliance matrix of the flexible skin model. After the compliance matrix constants are obtained, the linear elastic constants of the model can be calculated by the following expression:

$$\begin{gathered} E_x = 1/\bar{S}_{11}, \qquad E_y = 1/\bar{S}_{22}, \\ E_z = 1/\bar{S}_{33} \\ \nu_{xy} = -\bar{S}_{21}/\bar{S}_{11}, \qquad \nu_{xz} = -\bar{S}_{31}/\bar{S}_{11}, \\ \nu_{yz} = -\bar{S}_{23}/\bar{S}_{22} \\ G_{xy} = 1/\bar{S}_{66}, \qquad G_{xz} = 1/\bar{S}_{55}, \qquad G_{yz} = 1/\bar{S}_{44}. \end{gathered} \tag{2}$$

2.2. Stiffness matrix constants

According to the thick laminate theory [37], for a single composite system and unbalanced ply configuration, the stiffness matrix constants of the model can be simplified as:

$$\begin{aligned}
\bar{C}_{1i} &= \sum_{k=1}^{N} v_k \bar{C}_{1i}^{(k)} + \sum_{k=2}^{N} (\bar{C}_{13}^{(k)} - \lambda_{13}) v_k \\
&\quad \times (\bar{C}_{i3}^{(1)} - \bar{C}_{i3}^{(k)}) / \bar{C}_{33}^{(k)}, \qquad (i = 1, 2, 6) \\
\bar{C}_{2j} &= \sum_{k=1}^{N} v_k \bar{C}_{2j}^{(k)} + \sum_{k=2}^{N} (\bar{C}_{23}^{(k)} - \lambda_{23}) v_k \\
&\quad \times (\bar{C}_{j3}^{(1)} - \bar{C}_{j3}^{(k)}) / \bar{C}_{33}^{(k)}, \qquad (j = 2, 6) \\
\bar{C}_{l3} &= \sum_{k=1}^{N} v_k \bar{C}_{l3}^{(k)}, \qquad (l = 1, 2, 6) \\
\bar{C}_{33} &= 1 \Big/ \left(\sum_{k=1}^{N} v_k / \bar{C}_{33}^{(k)} \right) \\
\bar{C}_{mn} &= \left(\sum_{k=1}^{N} v_k \bar{C}_{mn}^{(k)} / \Delta_k \right) \Big/ \Delta, \qquad (m, n = 4, 5) \\
\bar{C}_{66} &= \sum_{k=1}^{N} v_k \bar{C}_{66}^{(k)} + \sum_{k=2}^{N} (\bar{C}_{36}^{(k)} - \lambda_{36}) v_k (\bar{C}_{36}^{(1)} - \bar{C}_{36}^{(k)}) / \bar{C}_{33}^{(k)}
\end{aligned} \tag{3}$$

where N indicates the total number of the laminate, and the terms λ_{13}, λ_{23}, λ_{36}, Δ and Δ_k can be expressed as:

$$\lambda_{13} = \bar{C}_{13}, \qquad \lambda_{23} = \bar{C}_{23}, \qquad \lambda_{36} = \bar{C}_{36} \tag{4}$$

$$\begin{aligned}
\Delta &= \left(\sum_{k=1}^{N} v_k \bar{C}_{44}^{(k)} / \Delta_k \right) \left(\sum_{k=1}^{N} v_k \bar{C}_{55}^{(k)} / \Delta_k \right) \\
&\quad - \left(\sum_{k=1}^{N} v_k \bar{C}_{45}^{(k)} / \Delta_k \right)^2
\end{aligned} \tag{5}$$

$$\Delta_k = \bar{C}_{44}^{(k)} \bar{C}_{55}^{(k)} - (\bar{C}_{45}^{(k)})^2 \tag{6}$$

where v_k is the volume fraction of the kth lamina and defined as $v_k = t_k/h$. The symbol t_k is the thickness of the kth lamina, h is the total thickness of the laminate.

2.3. Laminate-plate theory

The symbol $\bar{C}_{ij}^{(k)}$ stands for the off-axis stiffness matrix constants of the kth lamina. The off-axis stiffness constants in matrix $[\bar{C}_{ij}^{(k)}]$ can be obtained from the on-axis coordinate constants in matrix $[C_{ij}^{(k)}]$, as shown in figure 1, using a stiffness transformation matrix written as [38]:

$$[\bar{C}_{ij}^{(k)}] = [T^{\sigma}{}_{il}]^{-1} [C_{lm}^{(k)}] [T^{\varepsilon}{}_{mj}] \tag{7}$$

where matrix $[T^{\sigma}{}_{il}]$ and $[T^{\varepsilon}{}_{mj}]$ are respectively the base change of stress and strain. The stiffness constants of matrix $[C_{ij}^{(k)}]$ are given as follows [39]:

$$\begin{aligned}
\Delta &= \frac{1 - \mathrm{v}_{12}v_{21} - \mathrm{v}_{13}v_{31} - \mathrm{v}_{23}v_{32} - 2\mathrm{v}_{21}v_{13}\mathrm{v}_{32}}{E_{11}E_{22}E_{33}} \\
C_{11} &= \frac{1 - \mathrm{v}_{23}v_{32}}{E_{22}E_{33}\Delta}, \qquad C_{12} = \frac{v_{12} + v_{13}\mathrm{v}_{32}}{E_{11}E_{33}\Delta}, \\
C_{13} &= \frac{\mathrm{v}_{13} + v_{12}v_{23}}{E_{11}E_{22}\Delta} \\
C_{22} &= \frac{1 - \mathrm{v}_{13}v_{31}}{E_{11}E_{33}\Delta}, \qquad C_{23} = \frac{v_{23} + v_{21}\mathrm{v}_{13}}{E_{11}E_{22}\Delta}, \\
C_{33} &= \frac{1 - \mathrm{v}_{12}v_{21}}{E_{11}E_{22}\Delta} \\
G_{44} &= G_{23}, \qquad G_{55} = G_{31}, \qquad G_{66} = G_{12}.
\end{aligned} \tag{8}$$

While each layer of the laminated-plate exhibits the properties of fiber-reinforced composite materials, the matrix material is isotropic and fiber is transversely isotropic, its elastic constants can be obtained using a classical rule-of-mixture [40]:

$$\begin{aligned}
E_{11} &= V_{\mathrm{f}} E_{\mathrm{f}11} + V_{\mathrm{m}} E_{\mathrm{m}}, \\
E_{22} &= E_{33} = \frac{E_{\mathrm{f}22} E_{\mathrm{m}}}{E_{\mathrm{f}22} V_{\mathrm{m}} + E_{\mathrm{m}} V_{\mathrm{f}}} \\
G_{12} &= G_{13} = \frac{G_{\mathrm{f}12} G_{\mathrm{m}}}{G_{\mathrm{f}12} V_{\mathrm{m}} + G_{\mathrm{m}} V_{\mathrm{f}}}, \\
G_{23} &= \frac{G_{\mathrm{f}23} G_{\mathrm{m}}}{G_{\mathrm{f}23} V_{\mathrm{m}} + G_{\mathrm{m}} V_{\mathrm{f}}} \\
v_{12} &= v_{13} = V_{\mathrm{f}} v_{\mathrm{f}12} + V_{\mathrm{m}} v_{\mathrm{m}}, \\
v_{23} &= V_{\mathrm{f}} v_{\mathrm{f}23} + V_{\mathrm{m}} v_{\mathrm{m}},
\end{aligned} \tag{9}$$

where $E_{\mathrm{f}11}, E_{\mathrm{f}22}, G_{\mathrm{f}12}, G_{\mathrm{f}23}, v_{\mathrm{f}12}$ and $v_{\mathrm{f}23}$ are the material constants of the carbon fiber, E_{m}, v_{m} and G_{m} are the material constants of matrix, V_{f} and V_{m} are the volume fractions of fiber and matrix material.

3. Manufacturing and experimental testing

3.1. Flexible skin manufacturing

The flexible skin samples were manufactured using unidirectional carbon fiber sheets (IMS60 24K, Hexcel Corporation) and silicone elastomer (Sylgard 184, Dow Corning Corporation). The manufacturing process is similar to the fabrication of a one-dimensional morphing aircraft skin [12]. First, two outer elastomer face-sheets were obtained using Sylgard 184 mixed liquid (ratio of the base to curing agent = 10:1), which were vacuumed for an hour to remove the air bubbles, then poured into a flat plate mold with a thickness of 1.8 mm, and cured at 100 °C for an hour in the vacuum oven. Second, four carbon fiber layers with different fiber offset angles were obtained using unidirectional carbon fiber sheets (thickness: 0.36 mm), which were cut by a cutting machine (Genesis 2100, BLACK & WHITE Ltd), as shown in figure 2(a). The binder threads of the carbon fiber layers were removed to eliminate their effect on the skin stiffness. Then, the edges of

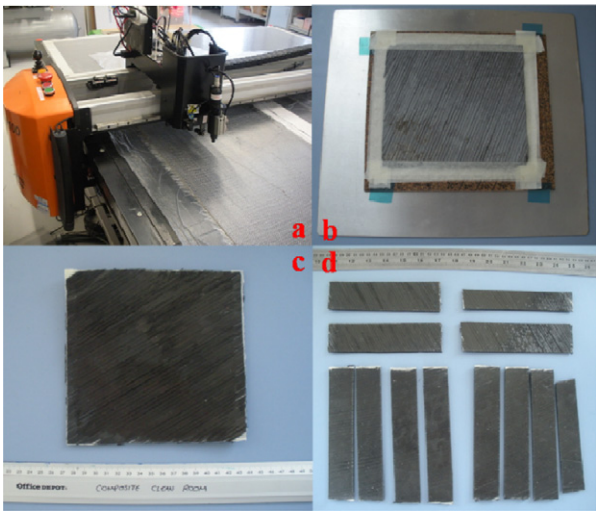

Figure 2. Manufacture schematic diagram of flexible skin.

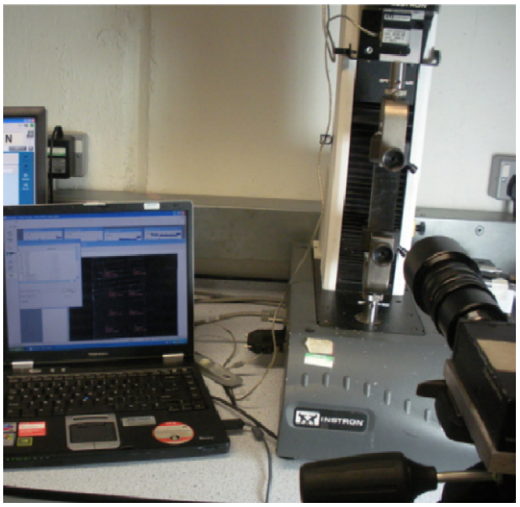

Figure 3. Flexible skin experimental setup.

the carbon fiber layer were fixed with masking tapes to ensure the relative position of the fiber strand (figure 2(b)). Finally, the prepared carbon fiber layers with different fiber offset angles and additional uncured elastomer were sandwiched between the two outer face-sheets, then moved to another flat plate mold with a thickness of 5 mm. After curing at 100 °C for an hour in the vacuum oven, a morphing skin sample with four layers of carbon fiber embedded in the elastomer matrix at $[\alpha/\beta]_S$ angle was obtained (figure 2(c)). The experimental specimens (dimensions of 150 mm × 35 mm × 5 mm) were obtained through cutting the morphing skin sample with a knife (figure 2(d)). The specimens had a fiber volume fraction of 0.228.

3.2. Tensile test

The elastic modulus along the x direction and in-plane Poisson's ratio of the morphing skin were obtained from the in-plane tensile test. The tensile tests were performed on a materials testing machine (Instron 3343, load cell: 1 kN) with a constant displacement rate of 0.5 mm min^{-1} (figure 3). The force and displacement values were recorded by BlueHill control and acquisition software. In order to improve the test accuracy, a video extensometer was used to record the accurate strain and displacement value. This system used a digital video camera (SONY XCD-X710) with a zoom lens (COMPUTAR 18-108/2.5) connected to a PC running Video Gauge software (IMETRUM Ltd). The positions (in pixels) of targets marked on the sample could be tracked and measured by the Video Gauge software during the testing. In order to obtain the actual displacement, a reference displacement was used to convert the pixels into actual metric values [41]. The sample actual strains along the x and y directions (ε_x and ε_y) could be obtained by respectively measuring the positions of any two targets along the x and y directions. Based on the measurement results, the in-plane Poisson's ratio could be obtained with its definition $\nu_{xy} = -\varepsilon_y/\varepsilon_x$.

4. Results and discussions

4.1. Comparison between experiments and analytical model

In order to study the in-plane Poisson's ratio and elastic modulus (along the x direction), two morphing skin samples with different fiber offset angles $[20/70]_S$ and $[30/60]_S$ were chosen and manufactured. Through measurement, the tensile specimens had the actual fiber offset angles of $[17/72]_S$ and $[31/60]_S$ after being cut by the knife. Since the unidirectional carbon fiber data sheet (IMS60, 24K) provided by the supplier was not enough to obtain its three-dimensional elastic constants, several other types of carbon fiber were chosen and the basic elastic constants of them were shown in table 1. It is worth noticing that the carbon fibers IMS 5131 and T800H have almost the same filament diameters (5 μm), axial Young's moduli (290 GPa) and tensile strengths (5.6 GPa) compared to carbon fiber IMS60, which was used as the reinforcing layer of the skin sample. The elastic modulus of the silicone elastomer (Sylgard 184) was determined from the tensile tests to have a value of 2.83 MPa. According to the research results of Yu and Zhao [42], the in-plane Poisson's ratio $\nu_m = 0.5$ is used in this work.

Table 2 shows the comparison of the elastic modulus E_x and in-plane Poisson's ratio ν_{xy} between theoretical and experimental results. The theoretical values are obtained based on a combination of the theoretical derivation and the basic material parameters of carbon fibers. The experimental values are the average values (four specimens) of in-plane tensile test results, which were obtained within the initial linear elastic range (2%–5%). An excellent agreement between theoretical results related to the four types of carbon fibers can be observed, which indicates that the difference of the carbon fiber types does not make any significant change to the elastic modulus (less than 0.03%) and in-plane Poisson's ratio (less than 0.05%) of the skin sample with such ply angle configurations. It could be attributed to the fact that both the theoretical results of elastic modulus and in-plane Poisson's ratio are not sensitive to the types of carbon fibers

Table 1. Basic material parameters of carbon fibers.

Fiber	Elastic modulus E_{11} (GPa)	Elastic modulus $E_{22=33}$ (GPa)	Shear modulus $G_{12=13}$ (GPa)	Poisson's ratio $\nu_{12=13}$	Poisson's ratio ν_{23}
T300[a]	231	13.8	12.4	0.2	0.25
IM7[b]	263.7	19.0	27.6	0.2	0.35
IMS 5131[c]	290	14.0	25.0[e]	0.236	0.011
T800H[d]	294	20.0	25.0	0.02	0.42

[a] Reference [43].
[b] Reference [44].
[c] Reference [45].
[d] Reference [46].
[e] Assumed: the same values as for the T800H.

Table 2. Comparison between theoretical and experimental results.

Fiber angle	Properties	T300	IM7	IMS 5131	T800H	Experiment
$[17/72]_S$	E_x (MPa)	28.387	28.390	28.391	28.392	33.038 ± 1.405
	ν_{xy}	−1.0614	−1.0616	−1.0617	−1.0617	-0.9197 ± 0.0803
$[31/60]_S$	E_x (MPa)	16.828	16.831	16.832	16.833	18.903 ± 2.908
	ν_{xy}	−0.9588	−0.9590	−0.9592	−0.9592	-0.9045 ± 0.0504

in such ply angles ($[17/72]_S$ and $[31/60]_S$), when the axial elastic modulus of carbon fiber is more than four orders of magnitude greater than the silicone elastomer. In addition, for the theoretical results of elastic modulus, the slight change (less than 0.03%) could also be ascribed to the relatively lower fiber volume fraction (0.228) of the skin. Good agreement is observed in general, with the theoretical values showing a reasonable decrease (14.06% and 10.95%) below the experimental results for the elastic modulus at the ply angles $[17/72]_S$ and $[31/60]_S$, while a reasonable increase (15.44% and 6.05%) over the experimental results for the in-plane Poisson's ratio at both ply angles. Uncertainties affecting the discrepancy between the experimental and analytical results can be ascribed to the fact that the material parameters used in the theoretical method are not exactly the same as the actual materials parameters of the experimental sample. According to Schneider [47], a high hardening temperature and long hardening time may result in an increase of the elastic modulus for Sylgard 184. Since the accuracy of the theoretical values have been validated by the experimental results, the material parameters related to carbon fiber T800H will be used in the following parametric analysis.

4.2. Parametric analysis

4.2.1. In-plane Poisson's ratio ν_{xy}. Figures 4(a)–(d) show the analytical predictions for the in-plane Poisson's ratio versus fiber angle $[\alpha/\beta]_S$ (where β is fixed and α is varied) for different fiber volume fractions when the matrix material has a lower elastic modulus ($E_m = 10$ MPa). As shown in figure 4(a), for increasing fiber volume fraction, the magnitude of Poisson's ratio first increases then decreases when the fiber angle α is kept constant, the maximum value occurs at $V_f = 0.5$, and the minimum value occurs at $V_f = 0.1$ and $V_f = 0.9$. The magnitude exhibits a symmetry about $V_f = 0.5$. A similar trend can also be observed in figures 4(b)–(d). For increasing fiber volume fraction (from 0.1 to 0.5), the analytical predictions show a corresponding maximum magnitude of Poisson's ratio increasing from 8.56 to 12.66 when the fiber angle $\beta = 10$ (figure 4(a)) and a corresponding maximum magnitude increasing from 15.18 to 26.54 when the fiber angle $\beta = 30$ (figure 4(b)). In addition, the corresponding maximum magnitude increases from 14.06 to 24.36 when the fiber angle $\beta = 50$ (figure 4(c)) and the corresponding value increases from 9.49 to 14.61 when the fiber angle $\beta = 70$ (figure 4(d)). It is worth noting that the Poisson's ratio is always positive when the fiber angle $\alpha = 0, 90$ and β. Furthermore, there are two obvious valleys in figure 4(a), which is different from the other three figures (figures 4(b)–(d)). Finally, for constant fiber angle β, the Poisson's ratios almost coincide with each other when the fiber angle α is greater than 45 in figure 4(a), while this is true when the fiber angle α is greater than 15 in the other three figures.

Figures 5(a)–(d) show the analytical predictions related to the in-plane Poisson's ratio versus fiber angle $[\alpha/\beta]_S$ (where β is fixed and α is varied) for different fiber volume fractions when the matrix material has a higher elastic modulus ($E_m = 1000$ MPa). Similarly, as shown in figure 5(a), for increasing fiber volume fraction, the magnitude of Poisson's ratio first increases then decreases when fiber angles α is kept constant, as can also be observed in figures 5(b)–(d). In contrast, the magnitude does not exhibit the symmetry about $V_f = 0.5$. For increasing fiber volume fraction (from 0.1 through 0.5 to 0.9), the corresponding maximum magnitude of Poisson's ratio first increases from 0.69 to 1.72 then decreases to 0.95 when the fiber angle $\beta = 10$ (figure 5(a)), while the corresponding value first increases from 0.32 to 0.70 then decreases to 0.44

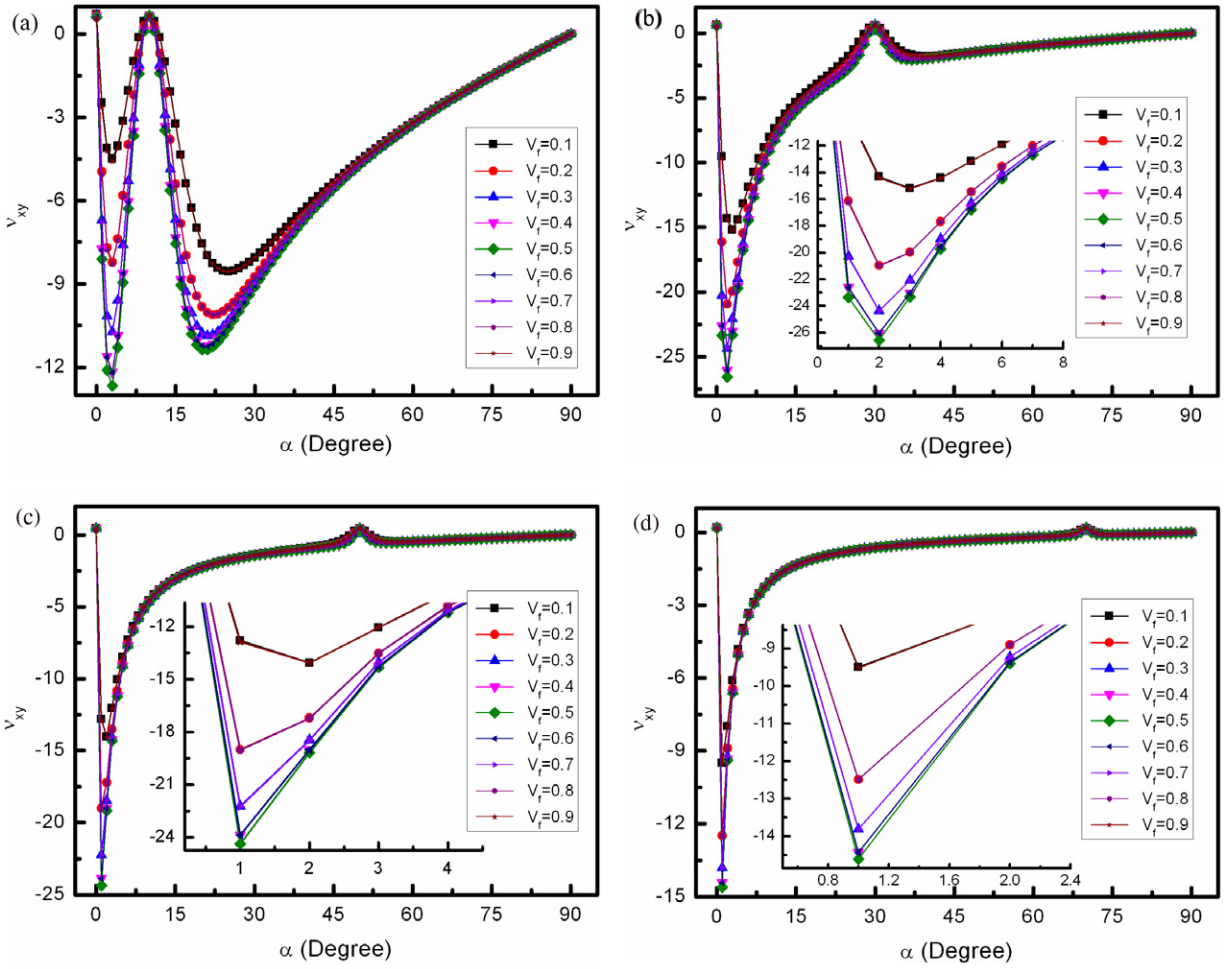

Figure 4. Analytical predictions for the in-plane Poisson's ratio ν_{xy} versus fiber angle α for different fiber volume fractions V_f ($E_m = 10$ MPa): (a) $\beta = 10$; (b) $\beta = 30$; (c) $\beta = 50$; (d) $\beta = 70$.

when the fiber angle $\beta = 30$ (figure 5(b)). In addition, the corresponding maximum magnitude first increases from 0.53 to 1.71 then decreases to 0.87 when the fiber angle $\beta = 50$ (figure 5(c)), and the corresponding value first increases from 0.65 to 1.39 then decreases to 0.80 when the fiber angle $\beta = 70$ (figure 5(d)). It can also be found that there are two obvious valleys in figure 5(b), which is different from the other three figures (figures 5(a), (c)–(d)). Moreover, the Poisson's ratio is positive when the fiber angle $\alpha = 0$, 90 and β.

Figures 6(a)–(d) show the analytical predictions for the in-plane Poisson's ratio versus fiber angle $[\alpha/\beta]_S$ (where β is fixed and α is varied) for different matrix elastic moduli when the fiber volume fraction is kept constant ($V_f = 0.5$). As shown in figure 6(a), the magnitude of Poisson's ratio decreases with increasing matrix elastic modulus when the fiber angle α is held constant. This can also be observed in figures 6(b)–(d). In general, for increasing matrix elastic modulus (from 5 to 1000 MPa), the analytical predictions show a corresponding maximum magnitude of Poisson's ratio decreasing from 23.09 to 1.72 when the fiber angle $\beta = 10$ (figure 6(a)), while the corresponding value decreases from 38.01 to 0.70 when the fiber angle $\beta = 30$ (figure 6(b)). In addition, the corresponding maximum magnitude decreases from 32.38 to 1.71 when the fiber angle $\beta = 50$ (figure 6(c)), and the corresponding value decreases from 17.18 to 1.38 when the fiber angle $\beta = 70$ (figure 6(d)).

The analytical predictions related to the in-plane Poisson's ratio ν_{xy} versus fiber angle α for different fiber angles β ($V_f = 0.5$, $E_m = 10$ MPa) are shown in figure 7. For all values of fiber angle α, it can be observed that the Poisson's ratio is positive when the fiber angle $\beta = 0$ and $\beta = 90$, which was verified by Peel [48]. In addition, the Poisson's ratio is also positive when the fiber angle $\beta = \alpha$. The maximum magnitude of Poisson's ratio (26.54) occurs at fiber angles $\beta = 30$ and $\alpha = 2$. From figure 7, it can be found that most of the higher magnitudes of Poisson's ratio are concentrated in the region $\alpha < 15$. Figure 8 shows the analytical predictions for the in-plane Poisson's ratio ν_{xy} versus fiber angle α for different fiber angles β ($V_f = 0.5$, $E_m = 1000$ MPa). In contrast to figure 7, the maximum magnitude of Poisson's ratio (1.72) is much lower in figure 8. It occurs at fiber angles $\beta = 10$ and $\alpha = 53$. Furthermore, most of the higher magnitudes of Poisson's ratio are not limited to the region for $\alpha < 15$, but dispersed in a large region. By comparison, it can be found that a significant change of the Poisson's ratio can be achieved through changing the matrix elastic modulus.

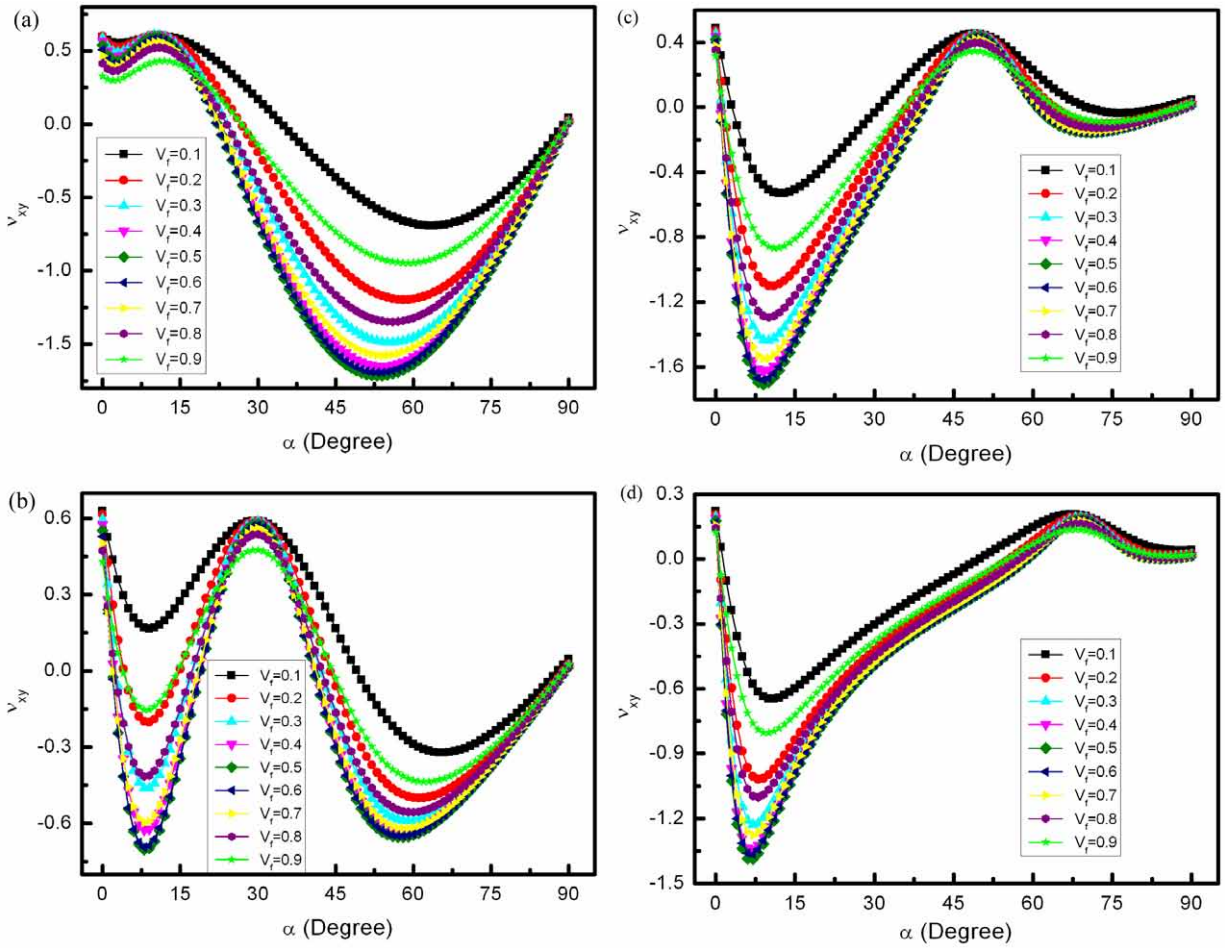

Figure 5. Analytical predictions for the in-plane Poisson's ratio ν_{xy} versus fiber angle α for different fiber volume fractions V_f ($E_m = 1000$ MPa): (a) $\beta = 10$; (b) $\beta = 30$; (c) $\beta = 50$; (d) $\beta = 70$.

4.2.2. Elastic modulus. Figure 9 shows the analytical predictions related to the elastic modulus E_x versus fiber angle α for different fiber angles β ($V_f = 0.5, E_m = 10$ MPa). For increasing fiber angle α, the elastic modulus decreases when the fiber angle β is kept constant (not including $\beta = 0$), except for a minimum value occurring at fiber angle $\alpha = \beta$. When fiber angle $\beta = 0$, for increasing fiber angle α, the elastic modulus first decreases rapidly, then approaches a asymptotic behavior. Similarly, when the fiber angle α is kept constant, the elastic modulus decreases with increasing fiber angle β, except for a minimum value occurring at fiber angle $\alpha = \beta$. A similar trend can also be observed in figure 10. Figure 10 shows the analytical predictions related to the elastic modulus E_x versus fiber angle α for different fiber angles β ($V_f = 0.5, E_m = 1000$ MPa). In comparison with the modulus variation around the region $\alpha = \beta$, the curve in figure 10 is less severe. It should be attributed to the fact that the stiffness ratio (E_{11}/E_{22}, equation (9)) in figure 10 is lower than that in figure 9. According to the study results of Peel [48], the stiffness ratio is one of the primary factors contributing to the negative Poisson's ratio of fiber-reinforced composites. Figure 11 shows the analytical predictions related to the stiffness ratio E_{11}/E_{22} versus fiber volume fraction V_f for different matrix elastic moduli E_m. For increasing fiber volume fraction, the stiffness ratio exhibits a trend of first increasing then decreasing when the matrix elastic modulus $E_m = 10$ MPa. The stiffness ratio value also exhibits a symmetry about $V_f = 0.5$, which explains the symmetry of the maximum magnitude related to Poisson's ratio in figure 4. In contrast, when the matrix elastic modulus $E_m = 1000$ MPa, the stiffness ratio value does not exhibit the symmetry about $V_f = 0.5$, which explains the reason why we cannot observe the symmetry of maximum magnitude related to Poisson's ratio about $V_f = 0.5$ in figure 5. Through observing figures 7–11, it could be found that it is possible to obtain larger selection ranges related to Poisson's ratio and elastic modulus with a higher stiffness ratio.

As shown in figure 9, since the variation curves of elastic modulus show the same trends for different fiber angles β, fiber angle $\beta = 70$ will be used in the following parametric discussion. Analytical predictions for the elastic modulus E_x versus fiber angle α for different fiber volume fractions V_f ($\beta = 70, E_m = 10$ MPa) are shown in figure 12. For increasing fiber volume fraction, the elastic modulus increases when fiber angle α is kept constant. As mentioned above, for constant fiber angle β, the Poisson's ratios almost coincide with each other when the fiber angle α is higher than 15 (figure 4(d)). However, the elastic moduli do not coincide with

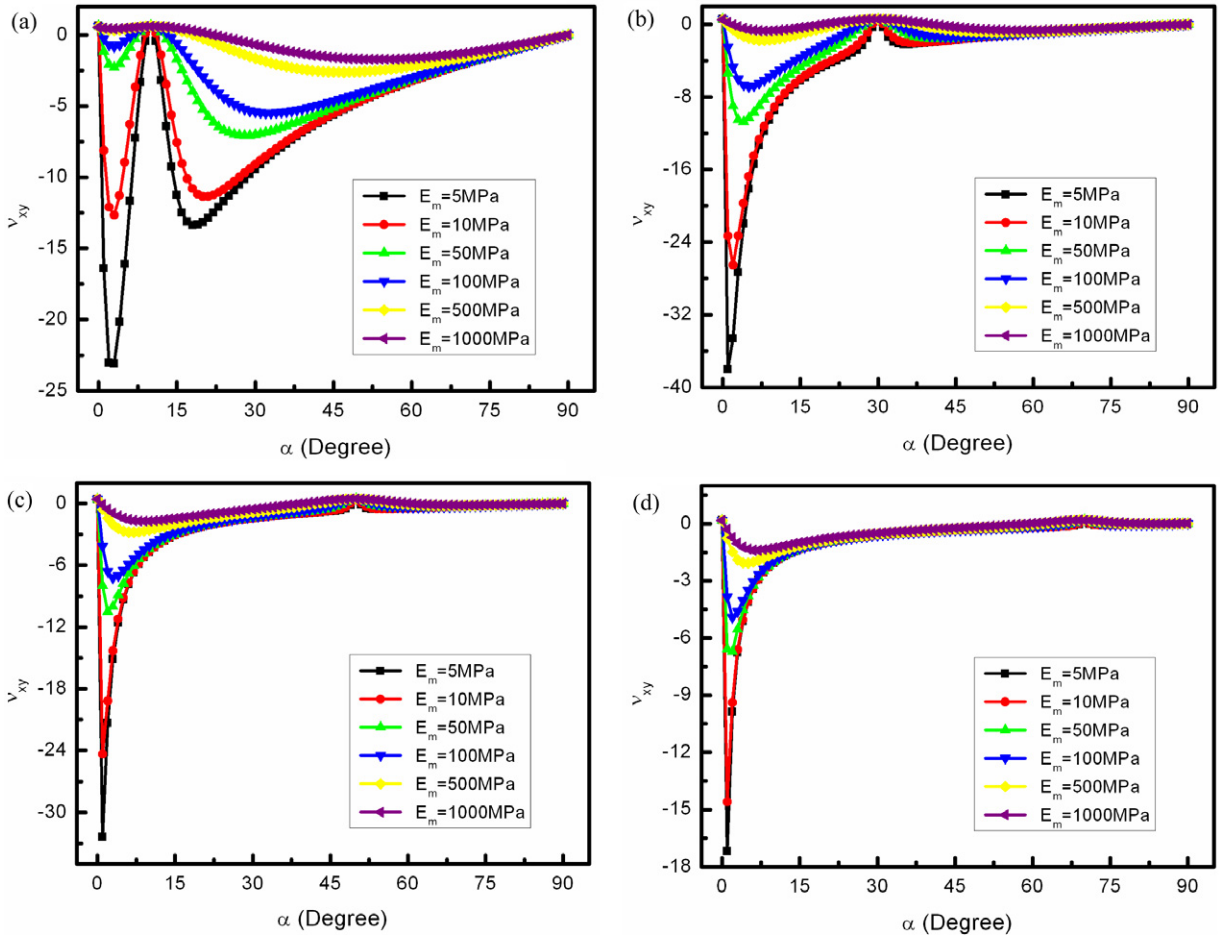

Figure 6. Analytical predictions for the in-plane Poisson's ratio ν_{xy} versus fiber angle α for different matrix elastic moduli E_{m} ($V_{\mathrm{f}} = 0.5$): (a) $\beta = 10$; (b) $\beta = 30$; (c) $\beta = 50$; (d) $\beta = 70$.

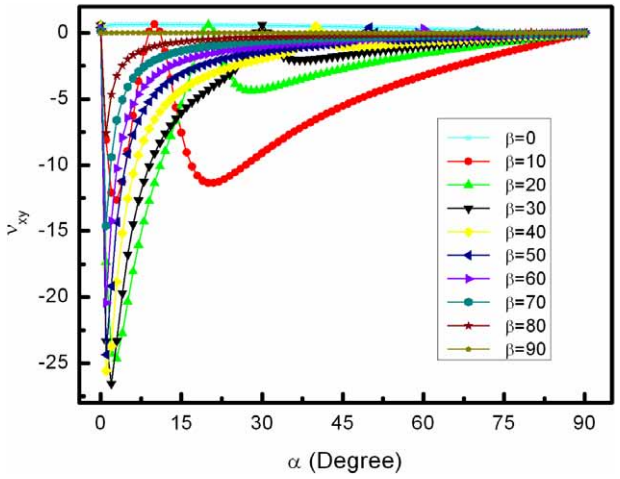

Figure 7. Analytical predictions for the in-plane Poisson's ratio ν_{xy} versus fiber angle α for different fiber angles β ($E_{\mathrm{m}} = 10$ MPa, $V_{\mathrm{f}} = 0.5$).

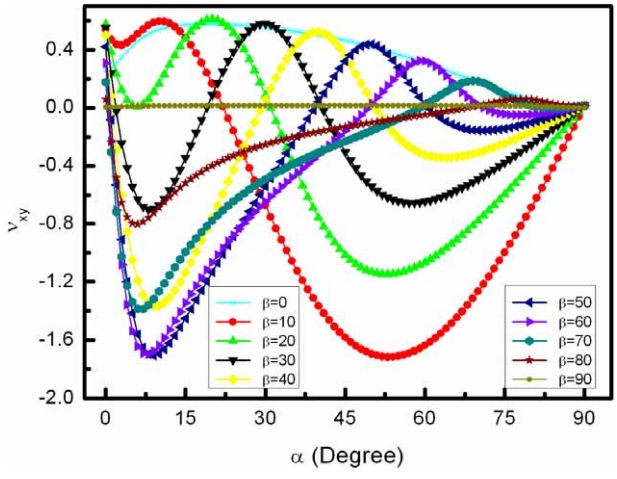

Figure 8. Analytical predictions for the in-plane Poisson's ratio ν_{xy} versus fiber angle α for different fiber angles β ($E_{\mathrm{m}} = 1000$ MPa, $V_{\mathrm{f}} = 0.5$).

each other under the same conditions (figure 12). The results suggest the possibility of using fiber-reinforced composites to design flexible skins with the same negative Poisson's ratios but different elastic moduli.

Figure 13 shows the analytical predictions related to the elastic moduli E_x and E_y versus fiber angle α for different fiber angles β ($V_{\mathrm{f}} = 0.5$, $E_{\mathrm{m}} = 10$ MPa). For simplicity, only four fiber angles β ($\beta = 10$, 30, 50 and 70) were chosen in

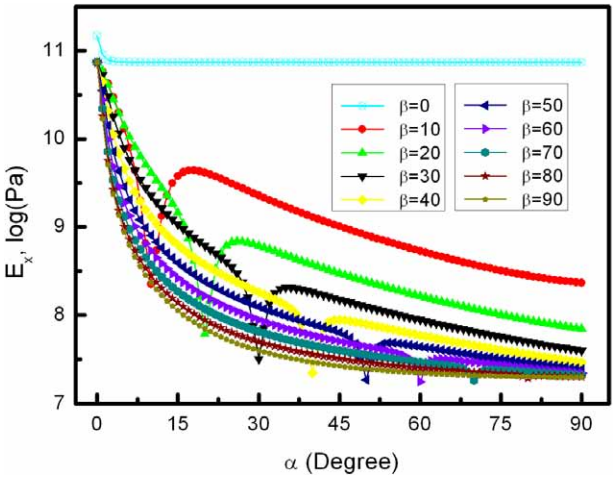

Figure 9. Analytical predictions for the elastic modulus E_x versus fiber angle α for different fiber angles β ($E_m = 10$ MPa, $V_f = 0.5$).

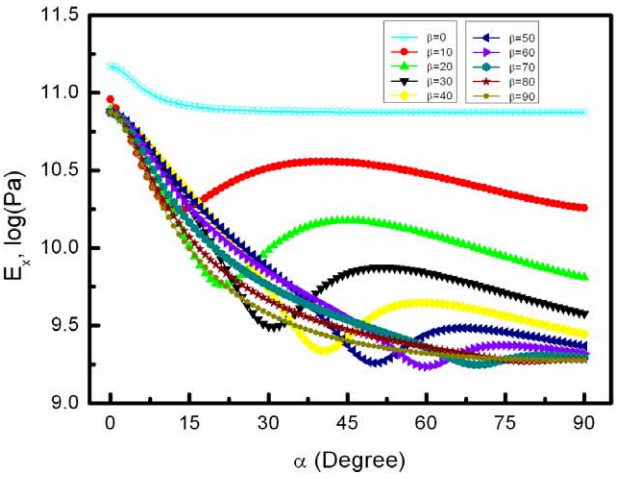

Figure 10. Analytical predictions for the elastic modulus E_x versus fiber angle α for different fiber angles β ($E_m = 1000$ MPa, $V_f = 0.5$).

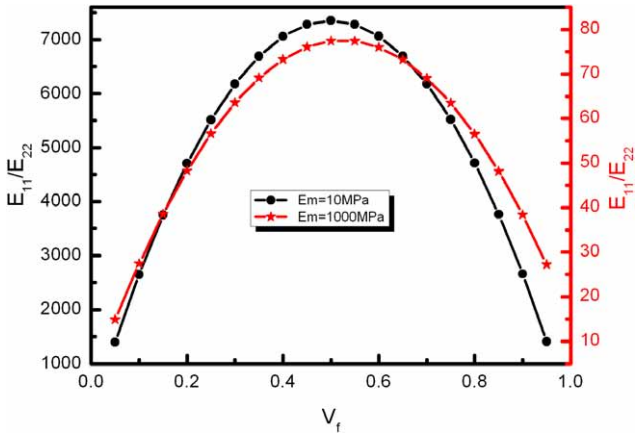

Figure 11. Analytical predictions for the stiffness ratio E_{11}/E_{22} versus fiber volume fraction V_f for different matrix elastic moduli E_m..

the following discussion. For increasing fiber angle α, the elastic modulus E_x tends to decrease when fiber angle β is kept constant, in contrast to the elastic modulus E_y increasing

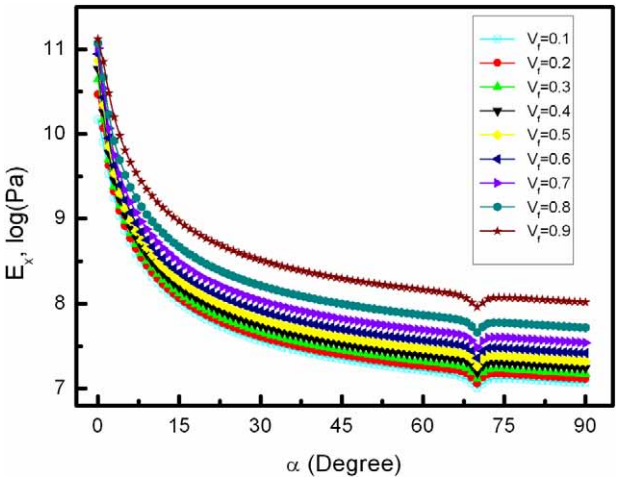

Figure 12. Analytical predictions for the elastic modulus E_x versus fiber angle α for different fiber volume fractions V_f ($\beta = 70$, $E_m = 10$ MPa).

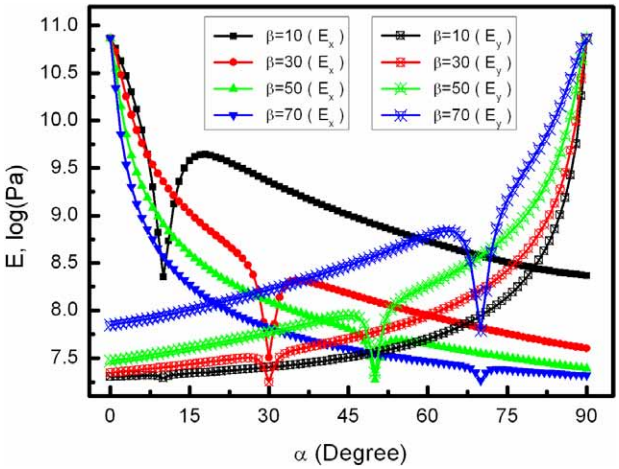

Figure 13. Analytical predictions for the elastic moduli E_x and E_y versus fiber angle α for different fiber angles β ($V_f = 0.5$, $E_m = 10$ MPa).

(figure 13). However, both elastic moduli E_x and E_y show their minimum values at fiber angle $\alpha = \beta$. In addition, it can be observed that the elastic moduli E_x and E_y show the same values at fiber angle $[\alpha/\beta]_S = [80/10]_S, [60/30]_S, [40/50]_S$ and $[20/70]_S$, respectively (figure 13). A similar trend can also be observed in figure 14, except the values of elastic moduli E_x and E_y in figure 14 are higher than those of figure 13. The analysis results suggest the possibility of using fiber-reinforced composites to design negative Poisson's ratio flexible skins with the same elastic modulus along the x and y directions.

4.2.3. Relation between in-plane Poisson's ratio and elastic modulus. Figure 15 shows the analytical predictions for the in-plane Poisson's ratio ν_{xy} versus elastic moduli E_x for different fiber angles β ($E_m = 10$ MPa, $V_f = 0.5$). In order to make these curves easy to distinguish from each other, two figures (figures 15(a) and (b)) were used to describe the

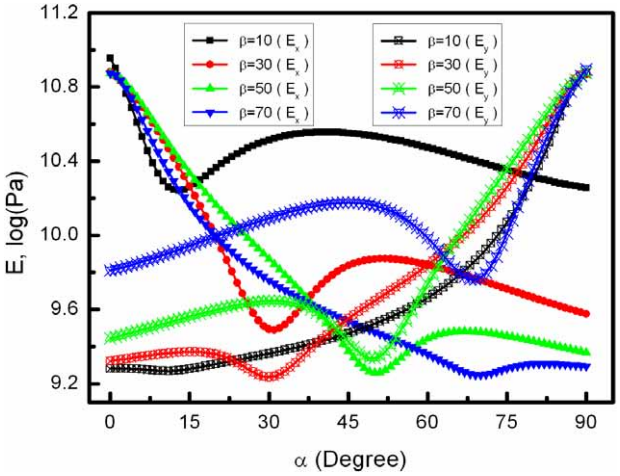

Figure 14. Analytical predictions for the elastic moduli E_x and E_y versus fiber angle α for different fiber angles β ($V_f = 0.5$, $E_m = 1000$ MPa).

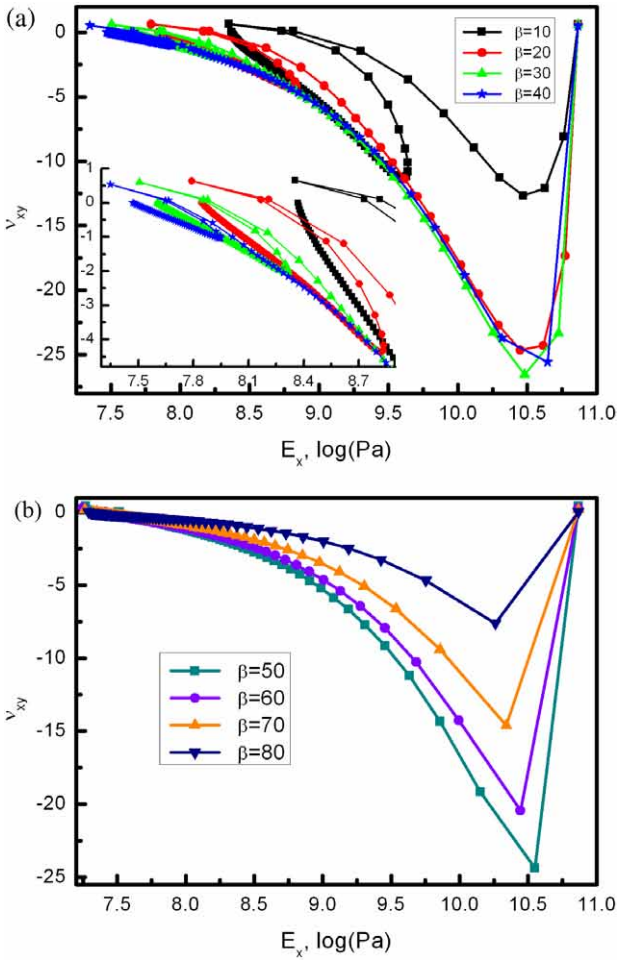

Figure 15. Analytical predictions for the in-plane Poisson's ratio ν_{xy} versus elastic moduli E_x for different fiber angles β ($E_m = 10$ MPa, $V_f = 0.5$): (a) $\beta = 10$, 20, 30 and 40; (b) $\beta = 50$, 60, 70 and 80.

relations between ν_{xy} and E_x. For decreasing values of the elastic modulus E_x and fibre angle β constant, the magnitude of the Poisson's ratio ν_{xy} presents a complex behavior, with a double increase/decrease over the Young's modulus range

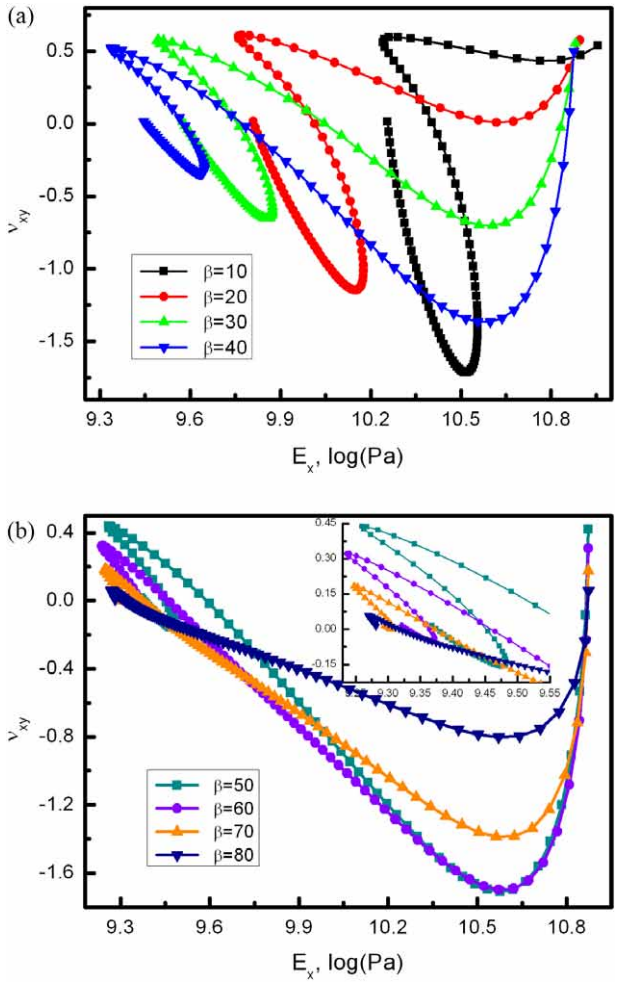

Figure 16. Analytical predictions for the in-plane Poisson's ratio ν_{xy} versus elastic moduli E_x for different fiber angles β ($E_m = 1000$ MPa, $V_f = 0.5$): (a) $\beta = 10$, 20, 30 and 40; (b) $\beta = 50$, 60, 70 and 80.

(figure 15). The three local minimum magnitude values occur at the fiber angle $\alpha = 0$, $\alpha = \beta$ and $\alpha = 90$, respectively. A similar trend can also be observed in figure 15(b). However, the trend of the second increase and decrease is not obvious in figure 15(b).

The analytical predictions for the in-plane Poisson's ratio ν_{xy} versus elastic moduli E_x for different fiber angles β ($E_m = 1000$ MPa, $V_f = 0.5$) are shown in figures 16(a) and (b). In comparison to figure 15, the trends of the Poisson's ratios are similar, but more obvious in figure 16. This is attributed to the fact that the range of values of Poisson's ratio in figure 16 is less than 10 times that in figure 15. By observing figures 15 and 16, it can be found that it is possible to obtain a flexible skin with the same in-plane negative Poisson's ratios but different elastic moduli, or the same elastic moduli but different in-plane negative Poisson's ratios.

5. Conclusions

In this work, a class of fiber-reinforced composite flexible skin with in-plane negative Poisson's ratio behavior has

been manufactured and investigated from an analytical and experimental point of view. The focus of this investigation was the relation between the in-plane Poisson's ratio and the material parameters. The accuracy of the theoretical model has been validated by the experimental results. A parametric analysis showed that significant changes in the in-plane negative Poisson's ratio could be achieved through changing the fiber ply angles and matrix elastic moduli. In addition, fiber-reinforced composite skins with the same in-plane negative Poisson's ratios but different elastic moduli, or the same elastic moduli but different in-plane negative Poisson's ratios could also be achieved through proper material parameter selection. The analysis presented in this work provides meaningful guidelines towards developing and manufacturing a new type of flexible skin with negative Poisson's ratios for morphing skin applications.

Acknowledgments

The Authors acknowledge the partial support of the European Project FP7-NMP-2009-LARGE-3M-RECT for the logistics of the manufacturing and experimental rigs. Y J Chen would also like to thank CSC (Chinese Scholarship Council) for funding his research work through the University of Bristol. Special thanks go also to the University of Bristol and Harbin Institute of Technology.

References

[1] Bowman J, Weisshaar T and Sanders B 2002 Evaluating the impact of morphing technologies on aircraft performance *Proc. 43rd AIAA/ASME/ASCE/AHS/ASC Structures, Structural Dynamics, and Materials Conf. (Denver, CO)*

[2] Gern F H, Inman D J and Kapania R K 2002 Structural and aeroelastic modeling of general planform wings with morphing airfoils *AIAA J.* **40** 628–37

[3] Sanders B, Eastep F and Forster E 2003 Aerodynamic and aeroelastic characteristics of wings with conformal control surfaces for morphing aircraft *J. Aircr.* **40** 94–9

[4] Chen Y, Yin W, Liu Y and Leng J 2011 Structural design and analysis of morphing skin embedded with pneumatic muscle fibers *Smart Mater. Struct.* **20** 085033

[5] Chen Y, Sun J, Liu Y and Leng J 2012 Experiment and analysis of fluidic flexible matrix composite (F2MC) tube *J. Intell. Mater. Syst. Struct.* **23** 279–90

[6] Thill C, Etches J, Bond I, Potter K and Weaver P 2008 Morphing skins *Aeronaut. J.* **112** 117–39

[7] Bettini P, Airoldi A, Sala G, Landro L D, Ruzzene M and Spadoni A 2010 Composite chiral structures for morphing airfoils: numerical analyses and development of a manufacturing process *Composites* B **41** 133–47

[8] Blondeau J, Richeson J and Pines D J 2003 Design, development and testing of a morphing aspect ratio wing using an inflatable telescopic spar *Proc. 44th AIAA/ASME/ASCE/AHS Structures, Structural Dynamics, and Materials Conf. (Norfolk, VA)*

[9] Bae J S, Seigler T M and Inman D J 2005 Aerodynamic and static aeroelastic characteristics of a variable-span morphing wing *J. Aircr.* **42** 528–34

[10] Neal D, Good M, Johnston C, Robertshaw H, Mason W and Inman D 2004 Design and wind-tunnel analysis of a fully adaptive aircraft configuration *Proc. 45th AIAA/ASME/ASCE/AHS/ASC Structures, Structural Dynamics and Materials Conf. (Palm Springs, CA)*

[11] Bartley-Cho J D, Wang D P, Martin C A, Kudva J N and West M N 2004 Development of high-rate, adaptive trailing edge control surface for the smart wing phase 2 wind tunnel model *J. Intell. Mater. Syst. Struct.* **15** 279–91

[12] Bubert E A, Woods B K S, Lee K, Kothera C S and Wereley N M 2010 Design and fabrication of a passive 1D morphing aircraft skin *J. Intell. Mater. Syst. Struct.* **21** 1699–717

[13] Thuwis G, Abdalla M and Gürdal Z 2010 Optimization of a variable-stiffness skin for morphing high-lift devices *Smart Mater. Struct.* **19** 124010

[14] Murray G, Gandhi F and Bakis C 2010 Flexible matrix composite skins for one-dimensional wing morphing *J. Intell. Mater. Syst. Struct.* **21** 1771–81

[15] Yin W L, Sun Q J, Zhang B, Liu J C and Leng J S 2008 Seamless morphing wing with SMP skin *Adv. Mater. Res.* **47** 97–100

[16] Joo J J, Reich G W and Westfall J T 2009 Flexible skin development for morphing aircraft applications via topology optimization *J. Intell. Mater. Syst. Struct.* **20** 1969–85

[17] Olympio K R and Gandhi F 2010 Flexible skins for morphing aircraft using cellular honeycomb cores *J. Intell. Mater. Syst. Struct.* **21** 1719–35

[18] Olympio K R and Gandhi F 2007 Zero-v cellular honeycomb flexible skins for one-dimensional wing morphing *Proc. 48th AIAA/ASME/ASCE/AHS/ASC Structures, Structural Dynamics, and Materials Conf. (Honolulu, HI, April)*

[19] Bitzer T 1997 *Honeycomb Technology: Materials, Design, Manufacturing, Applications and Testing* (London: Chapman and Hall)

[20] Alderson A, Alderson K, Chirima G, Ravirala N and Zied K 2010 The in-plane linear elastic constants and out-of-plane bending of 3-coordinated ligament and cylinder-ligament honeycombs *Compos. Sci. Technol.* **70** 1034–41

[21] Alderson A *et al* 2010 Elastic constants of 3-, 4- and 6-connected chiral and anti-chiral honeycombs subject to uniaxial in-plane loading *Compos. Sci. Technol.* **70** 1042–8

[22] Gibson L J and Ashby M F 1997 *Cellular Solids: Structure and Properties* 2nd edn (Cambridge: Cambridge University Press)

[23] Bezazi A, Scarpa F and Remillat C 2005 A novel centresymmetric honeycomb composite structure *Compos. Struct.* **71** 356–64

[24] Evans K 1991 The design of doubly curved sandwich panels with honeycomb cores *Compos. Struct.* **17** 95–111

[25] Lakes R 1987 Foam structures with a negative Poisson's ratio *Science* **235** 1038–40

[26] Masters I and Evans K 1996 Models for the elastic deformation of honeycombs *Compos. Struct.* **35** 403–22

[27] Evans K E and Alderson A 2000 Auxetic materials: functional materials and structures from lateral thinking! *Adv. Mater.* **12** 617–28

[28] Evans K and Alderson K 2000 Auxetic materials: the positive side of being negative *Eng. Sci. Educ. J.* **9** 148–54

[29] Martin J, Heyder-Bruckner J J, Remillat C, Scarpa F, Potter K and Ruzzene M 2008 The hexachiral prismatic wingbox concept *Phys. Status Solidi* b **245** 570–7

[30] Spadoni A, Ruzzene M and Scarpa F 2006 Dynamic response of chiral truss-core assemblies *J. Intell. Mater. Syst. Struct.* **17** 941–52

[31] Bornengo D, Scarpa F and Remillat C 2005 Evaluation of hexagonal chiral structure for morphing airfoil concept *Proc. Inst. Mech. Eng.* G **219** 185–92

[32] Scarpa F, Smith F C, Chambers B and Burriesci G 2003 Mechanical and electromagnetic behaviour of auxetic honeycomb structures *Aeronaut. J.* **107** 175–83

[33] Hassan M, Scarpa F, Ruzzene M and Mohammed N 2008 Smart shape memory alloy chiral honeycomb *Mater. Sci. Eng.: A* **481** 654–7
[34] Spadoni A and Ruzzene M 2007 Numerical and experimental analysis of the static compliance of chiral truss-core airfoils *J. Mech. Mater. Struct.* **2** 965–81
[35] Heo H, Ju J, Kim D M and Jeon C S 2011 Passive morphing airfoil with honeycombs *Proc. ASME 2011 Int. Mechanical Engineering Congress & Exposition (IMECE) (Denver, CO, Nov.)*
[36] Dong W J and Sun Q 2011 Airfoil design and numerical analysis for morphing wing structure *Adv. Mater. Res.* **228** 169–73
[37] Sun C and Li S 1988 Three-dimensional effective elastic constants for thick laminates *J. Compos. Mater.* **22** 629–39
[38] Bakaiyan H, Hosseini H and Ameri E 2009 Analysis of multi-layered filament-wound composite pipes under combined internal pressure and thermomechanical loading with thermal variations *Compos. Struct.* **88** 532–41
[39] Hamed A F, Megat M, Sapuan S and Sahari B 2008 Theoretical analysis for calculation of the through thickness effective constants for orthotropic thick filament wound tubes *Polym.-Plast. Technol. Eng.* **47** 1008–15
[40] Šmilauer V, Hoover C G, Bažant Z P, Caner F C, Waas A M and Shahwan K W 2011 Multiscale simulation of fracture of braided composites via repetitive unit cells *Eng. Fract. Mech.* **78** 901–18
[41] Thill C, Etches J A, Bond I P, Weaver P M and Potter K D 2008 Experimental and parametric analysis of corrugated composite structures for morphing skin applications *Proc. 19th Int. Conf. on Adaptive Structures and Technologise (ICAST) (Ascona, Switzerland, Oct.)*
[42] Yu Y S and Zhao Y P 2009 Deformation of PDMS membrane and microcantilever by a water droplet: comparison between Mooney–Rivlin and linear elastic constitutive models *J. Colloid Interface Sci.* **332** 467–76
[43] Chen C H and Cheng C H 1996 Effective elastic moduli of misoriented short-fiber composites *Int. J. Solids Struct.* **33** 2519–39
[44] Case A A 2004 Permeability of hybrid composites subjected to extreme thermal cycling and low-velocity impacts *MS Thesis* Georgia Institute of Technology
[45] Koissin V *et al* 2009 Structurally stitched woven preforms: experimental characterisation, geometrical modelling, and FE analysis *Plast. Rubber Compos.* **38** 98–105
[46] Honjo K 2003 Fracture toughness of PAN-based carbon fibers estimated from strength-mirror size relation *Carbon* **41** 979–84
[47] Schneider F, Fellner T, Wilde J and Wallrabe U 2008 Mechanical properties of silicones for MEMS *J. Micromech. Microeng.* **18** 065008
[48] Peel L 2007 Exploration of high and negative Poisson's ratio elastomer-matrix laminates *Phys. Status Solidi* b **244** 988–1003